LIMNOLOGY
and
OCEANOGRAPHY: METHODS

ASLO

Limnol. Oceanogr.: Methods 19, 2021, 566–577

doi: 10.1002/lom3.10449

Quantifying upwelling in tropical shallow waters: A novel method using a temperature stratification index

Robin Guillaume-Castel,[1]* **Gareth J. Williams**,[1]* **Justin S. Rogers**,[2] **Jamison M. Gove**,[3] **J. A. Mattias Green**[1]

[1]School of Ocean Sciences, Bangor University, Anglesey, UK
[2]Environmental Fluid Mechanics Laboratory, Stanford University, Stanford, California
[3]Pacific Islands Fisheries Science Center, National Oceanic and Atmospheric Administration, Honolulu, Hawaii

Abstract

Upwelling has profound effects on nearshore tropical ecosystems, but our ability to study these patterns and processes depends on quantifying upwelling dynamics in a repeatable and rigorous manner. Previous methods often lack the ability to identify individual cold-pulse events within temperature time series data or require several user-defined parameters, and therefore previous hydrographic knowledge of the study site. When unavailable, parameters are chosen arbitrarily or from previous studies potentially conducted under different environmental contexts. Previous methods also require the user to manually separate upwelling-induced cold-pulse events from those caused by other physical mechanisms like surface downwelling. Here, we present a novel method that uses a temperature stratification index (TSI) to detect upwelling-induced cold-water intrusions in tropical waters. We define a cold pulse as a continuous period having an abnormally low TSI, with this criterion based on a climatological threshold of the temperature profile at the study site calculated from the National Centers for Environmental Prediction's Global Ocean Data Assimilation System (GODAS) reanalysis product. Our TSI method is therefore automatically tuned for the study site in question, removing biases associated with user-defined input parameters. The method also automatically determines the directional origin of the cold-water mass to isolate upwelling-induced cooling and can achieve overall cold-pulse detection rates 10–14.2% higher than previous methods. Our new TSI method can easily be adapted to detect a range of physical processes in shallow waters, including intrusion of water masses through upwelling, downwelling, and horizontal advection.

Temperature variations in the ocean can occur over various temporal scales. For example, they occur over years due to circulation changes (McPhaden et al. 2006), over months due to seasonal differences in surface layer warming (Rao and Sivakumar 2000), and at daily to sub-daily frequencies due to temporary changes in the physical properties of the water column and the diurnal solar cycle (Safaie et al. 2018). These latter short-term intrusions of cold water can affect a range of ecosystem patterns and processes. On tropical coral reefs, for example, short-term upwelling events can redistribute larvae, plankton, and nutrients throughout the water column (Pineda 1991; Leichter et al. 1996; Sevadjian et al. 2012), creating spatial disparities in resource supply that affect the growth rates of reef organisms (Leichter and Genovese 2006), their patterns of abundance (Aston et al. 2019), and their feeding ecology (Roder et al. 2010; Pacherres et al. 2013; Williams et al. 2018; Radice et al. 2019). Upwelling can also create temporary thermal refugia during abnormally high ocean temperature conditions (Reid et al. 2019; Wyatt et al. 2020) that can buffer the ecological impacts of mass coral bleaching and mortality (Wall et al. 2012; Schmidt et al. 2016; Safaie et al. 2018; Randall et al. 2020). Given these strong links between high-frequency temperature variations and the ecology of shallow-water tropical communities, we require a replicable method to quantify short-term cooling events.

Previous methods to quantify in situ cooling associated with upwelling from temperature time-series data consist of integrating all temperature values below a daily threshold, such as the daily mean (Leichter and Genovese 2006) or mode (most found temperature value in a day, e.g., Wall et al. 2012;

*Correspondence: r.guilcas@outlook.com and g.j.williams@bangor.ac.uk

Author Contribution Statement: R.G.C., G.J.W., and J.A.M.G. designed the study. R.G.C. developed the method with important feedback from all authors. J.M.G. and J.S.R. provided the data used for method development. R.G.C., G.J.W., and J.A.M.G. wrote the manuscript and all authors contributed to the editing of the manuscript.

Schmidt et al. 2016). The resulting metric of degree cooling days is then simply a sum of all cooling times across the entire temperature time series. A second method used by Wyatt et al. (2020) quantified cooling associated specifically with internal wave activity. Internal waves are subsurface gravity waves that break and dissipate energy at depth and by doing so, drive deep cooler water up into the warmer shallows (Alford et al. 2015; Woodson 2018). By filtering the temperature time series to retain all variability associated with frequencies between the local inertial frequency and the time-series sampling rate, Wyatt et al. (2020) identified cooling assumed to be linked to internal wave-induced upwelling. The aim of this method was not to quantify upwelling dynamics per se, but to quantify the overall temperature reprieve internal wave-induced upwelling affords shallow-water reefs during thermal stress events. However, the methods developed by Leichter and Genovese (2006) and Wyatt et al. (2020) have some limitations. Firstly, they give a summed value of high-frequency temperature cooling across an entire time series, but do not allow for the identification and timing of individual cold-pulse events. Secondly, they do not identify the directional origin of the cold-water mass. Wyatt et al. (2020) assumed that all high-frequency temperature drops occurred as a result of deep-water internal waves. This is not always the case when cold surface water sinks down through the water column as a result of a thermally driven gravity current following cold, possibly nocturnal, atmospheric conditions (Monismith et al. 2006; Williams et al. 2018).

An automated method to identify individual cold pulses in temperature time-series data was first presented by Sevadjian et al. (2012) and, to date, has been the most widely adopted method in tropical coral reef research (Gove et al. 2015; Williams et al. 2018; Aston et al. 2019; Comfort et al. 2019). The original method defines a cold pulse as whenever the temporal temperature gradient drops below a defined threshold (Sevadjian et al. 2012). If the temperature gradient stays below this threshold and the final temperature drop is greater than a specified value, a cold pulse is recorded. The event ends when the temperature recovers to a given fraction of its overall drop. There have been adaptations of the Sevadjian et al. (2012) method, including only identifying cold pulses with durations less than 13 h to focus on cooling events associated with semidiurnal tidal and supertidal frequencies (Gove et al. 2015; Williams et al. 2018), and those with a defined temperature drop occurring over a defined amount of time; then, the gradient did not have to be maintained (Comfort et al. 2019). In Williams et al. (2018) and Comfort et al. (2019), the routine was applied to subsurface temperature recorders in a depth array at the same location. If the cold pulse was recorded in an upslope direction (i.e., recorded first in the deepest logger and then sequentially up into the shallows), it was attributed to upwelling induced by internal waves. However, if the reverse was seen and the cooling occurred first in the shallows and transitioned across the loggers in a downslope direction, the cooling was attributed to surface downwelling (Williams et al. 2018).

Here, we will refer to the Sevadjian et al. (2012) method and its adaptations as the constant gradient threshold (CGT) method, because the temperature gradient threshold for defining a cold pulse remains the same throughout the time series. CGT methods are defined by four parameters: a gradient threshold, a minimum temperature drop, the overall temperature drop fraction that has to recover to mark the pulse end, and a maximum pulse duration. These parameters must be defined a priori, meaning cold-pulse detection ultimately depends on these somewhat arbitrary parameter choices. For example, a cold pulse can be easily missed if it shows a final temperature drop smaller than the defined minimum temperature drop. The CGT methods also do not automatically detect the directional origin of each cooling event and these must be manually identified from the temperature records, making it a labor-intensive process for isolating upwelling-induced cooling. It would therefore be beneficial to have a standardized way of defining the parameters based on the geographic location and time of the study, and an automated way to isolate and quantify cooling events related to upwelling. Here, we present a new method that achieves this when applied to in situ temperature time-series data collected across depths in shallow tropical waters, like those around tropical coral reefs.

Materials and procedures

Data

For method development, we used two temperature records from two locations in the Pacific Ocean. The first spanned 1 yr from April 17, 2015 to April 17, 2016 at three depths (6, 14, and 26 m) at a single location on the north outer reef slope (reef habitat facing the open ocean) of Palmyra Atoll in the central Pacific (5°53′49″N, 162°04′41″W) (Fig. 1a). The second record spanned 1 month from March 17 to April 16, 2014 at three depths (6, 14, and 25 m) on the north outer reef slope of Wake Atoll in the northwestern Pacific (19°18′58″N, 166°37′38″E) (Fig. 1b). The spatial configurations of the sensors and their relative distances apart on the reef were similar at both locations (Fig. 2a,b). For both records, measurements were taken using Sea-Bird Electronics© subsurface temperature recorders (SBE 56) attached to the reef floor and sampling every 5 min with an accuracy of 0.002°C. The data used were collected by the Ecosystem Sciences Division of the National Oceanic and Atmospheric Administration Pacific Island Fisheries Sciences Center's Pacific Reef and Monitoring Program. In the top 50 m, the temperature at Palmyra, closer to the Equator, is more than 1°C warmer than at Wake but the temperature decreases faster at Palmyra, typical of a shallower upper mixed layer depth (Fig. 2c). These slightly contrasting tropical

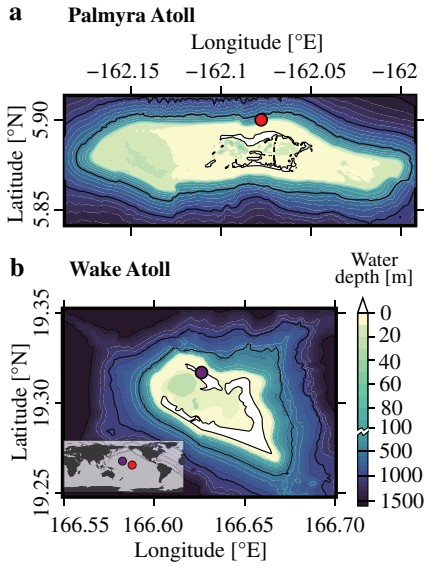

Fig 1. (**a**) Bathymetry of Palmyra Atoll and our study site (red circle) on the north outer reef slope. (**b**) Bathymetry of Wake Atoll and our study site (purple circle) and the location of Palmyra and Wake in the Pacific Ocean. Bathymetry data from Palmyra are derived from multibeam bathymetry surveys collected by NOAA's Pacific Islands Benthic Habitat Mapping Center (up to 25 m) and IKONOS satellite data (shallower than 25 m), available at http://www.soest.hawaii.edu/pibhmc/cms/data-by-location/pacific-remote-island-area/. Bathymetry data from Wake are also derived from multibeam bathymetry surveys collected by NOAA's Pacific Islands Benthic Habitat Mapping Center combined with satellite imagery and the General Bathymetry Chart of the Ocean (GEBCO, https://www.gebco.net/) product. Solid lines represent the 0-, 500-, 1000-, and 1500-m bathymetry contour lines.

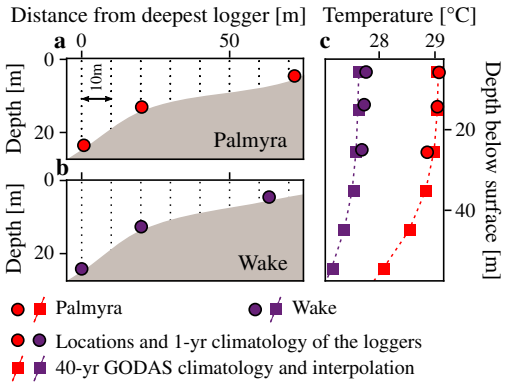

Fig 2. Spatial configuration and relative positioning of the temperature loggers producing the test dataset at Palmyra and Wake Atolls (**a**, **b**). (**c**) The 40-yr temperature climatology from the Global Ocean Data Assimilation System (GODAS) reanalysis product and its interpolation between depths (dashed lines), along with 1 yr mean temperature of in situ data at Palmyra and Wake.

water environments allow for a more robust assessment of our new method.

Method

In warm tropical marine waters, near-surface stratification variability can be linked to several processes including the presence of a cool and dense internal tidal bore (Leichter and Genovese 2006; Reid et al. 2019). An internal tidal bore is a gravity current formed by breaking internal wave. The bore strength proxy, used in Walter et al. (2014) and based on a stratification index (Simpson and Pingree 1978), indicates the magnitude of an internal bore. The proxy is calculated as the difference between the potential energy of the water column if it was fully mixed and the potential energy of the observed water column divided by the height of the water column. Physically, the bore strength proxy represents the energy required, per meter of depth, to fully mix the whole water column. Cold water intrusion, or cold pulses, in a warm tropical environment should therefore be detectable using a temperature proxy similar to the bore strength proxy.

In the following equations, depth averaged quantities are overlined ($\bar{\rho}$). The bore strength proxy for a water column at a time t, $\phi(t)$, is defined as (Walter et al. 2014):

$$\phi(t) = \frac{-g}{H}\int_0^H (\rho(z,t) - \bar{\rho}(t))z dz \quad (1)$$

where $g = 9.81$ m s^{-2} is the gravitational acceleration, H is the water column height, $\rho(z, t)$ is the instantaneous density at a depth z and time t, and $\bar{\rho}(t)$ is the mean profile density. To detect cold-water intrusion in a water column, we adapt Eq. 1 to give a temperature stratification index (TSI), ϕ_T, defined as:

$$\phi_T(t) = \frac{1}{H}\int_0^H \left(T(z,t) - \bar{T}(t)\right)z dz \quad (2)$$

Note Eqs. 1 and 2 are analogous and different only by a constant multiplier ($\phi \propto \phi_T$) if the density in Eq. 1 is primarily a function of temperature ($\rho \propto -T$), which is reasonable for shallow reef environments with few freshwater sources. In Eq. 2, $T(z, t)$ is the temperature time series of the vertical temperature structure and $\bar{T}(t)$ is the depth-averaged temperature time series. If the temperature data are discrete over n equally spaced depth levels, z_1, z_2, …, z_n, Eq. 2 can be written, using a midpoint Riemann sum, as:

$$\phi_T(t) = \frac{1}{n}\sum_{i=1}^{n}\left(T(z_i,t) - \bar{T}(t)\right)z_i = \overline{\left(T(z,t) - \bar{T}(t)\right)z} \quad (3)$$

In the following, Eq. 3 is used for almost equally spaced data.

The TSI is negative in a water column where the temperature is decreasing with depth. For a water column with a quasi-homogeneous temperature distribution, the TSI is close to zero. The TSI decreases as the temperature becomes more stratified as a result of cold-water intrusion at the bottom of the water column and the strength of the intrusion is quantified by the magnitude of the TSI. However, if the TSI is applied to a strictly vertical array of depths (e.g., sensors attached to a mooring), both upwelling and downwelling cold pulses will

either only affect the deepest logger or several loggers simultaneously. The best way to incorporate the direction of cold pulses would therefore be to use an array of bed-mounted loggers going upslope. The TSI would then be applied to the vertical projection of the bed-mounted array (Fig. 3) (note that the horizontal distance between loggers is not considered in the TSI computation as it is designed to compare the current vertical stratification to its background value).

In summary, our novel TSI method detects and quantifies upwelling-induced cold pulses in a warm, weakly stratified environment from an upslope array of temperature time-series data (Fig. 4). The step-by-step process is as follows and we provide detailed descriptions of the methods behind each step below:

Step 1 – Detecting potential cold pulses: For each time step, we compute the TSI for the water column and extract potential cold pulses as being periods where the TSI remains below a location-specific threshold.

Step 2 – Capturing the full extent of cold pulses detected: Potential pulses detected only encapsulate the part of the pulses with the strongest stratification. We therefore expand the boundaries of those potential pulses to capture their whole extent.

Step 3 – Filtering out potential cold pulses linked to surface heating: Heating of the surface layer may also induce temperature stratification of the water column that can show up as a potential pulse. We therefore filter potential pulses linked to heating at the shallowest logger using a custom-made heating filter.

Step 4 – Separating series of cold pulses: In the eventuality of several successive pulses detected, the event is broken down into individual pulses. Potential pulses remaining at that stage are considered true upwelling-induced cold pulses.

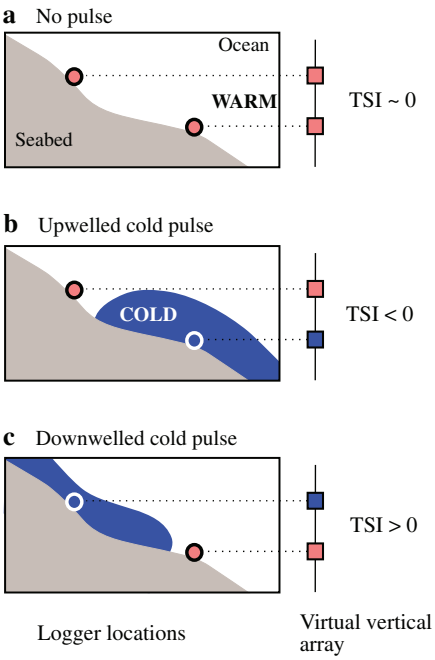

Fig 3. Schematic representation of how cold pulses affect the TSI computed from two temperature loggers in an upslope configuration. The TSI is computed on the virtual vertical array, which is the vertical projection of the actual logger locations on the seabed. (**a**) No pulse: The TSI is almost null. (**b**) Upwelled cold-pulse situation; the TSI computed is negative. (**c**) Downwelled cold pulse: The TSI computed is positive.

Detailed description of the method steps

Step 1: Detecting potential cold pulses

An upwelling-induced cold pulse should first cause a sharp temperature drop at the deepest logger in the array before propagating up the reef slope to shallower depths. The lag between the temperature drops at different depths causes a noticeable temperature stratification captured by a negative TSI. A potential upwelling-induced cold pulse is defined as a continuous period of TSI below a certain threshold. To compute a locally relevant TSI threshold, we use in-depth monthly temperature data from the National Center for Environmental Prediction Global Ocean Data Assimilation System reanalysis product (NCEP/GODAS; Behringer and Xue (2004)), available from https://psl.noaa.gov/data/gridded/data.godas.html. GODAS temperature data are monthly means covering the whole globe from 1980 to 2020, with a spatial resolution of 0.333° latitude × 1° longitude, across 40 depth levels in 10-m increments from 5 to 225 m depth. From the GODAS data, our routine computes the location-specific climatological mean and standard deviation of the TSI. It first extracts the temperature time series from the GODAS data at the closest data point to our location (for our test dataset: 5°50′N–162°30′W, 47 km away from our location). Then, the extracted data are interpolated to the depths of the subsurface temperature recorders and the TSI time series is computed for our temperature time series. The routine then uses the TSI time series to compute a 40-yr climatological mean TSI and standard deviation and defines an abnormally low TSI as a TSI lower than the climatological mean minus one standard deviation. The temperature climatology extracted from GODAS does not deviate much from the local 1-yr mean temperature computed from the sensors (Fig. 2c). The TSI threshold, θ, is therefore defined as:

$$\theta = \overline{\phi_{T-\mathrm{GODAS}}} - \sigma(\phi_{T-\mathrm{GODAS}}) \quad (4)$$

In Eq. 4, $\overline{\phi_{T-\mathrm{GODAS}}}$ is the 40-yr climatological mean TSI and $\sigma(\phi_{T-\mathrm{GODAS}})$ the 40-yr climatological standard deviation. Using the threshold θ in Eq. 4, a list of the start and end times of potential cold pulses within the temperature time-series data can be computed.

Step 2: Capturing the full extent of cold pulses detected

The potential cold pulses detected only represent the part of the pulses where the TSI magnitude is the strongest. To capture the full extent of the pulses, our routine defines new

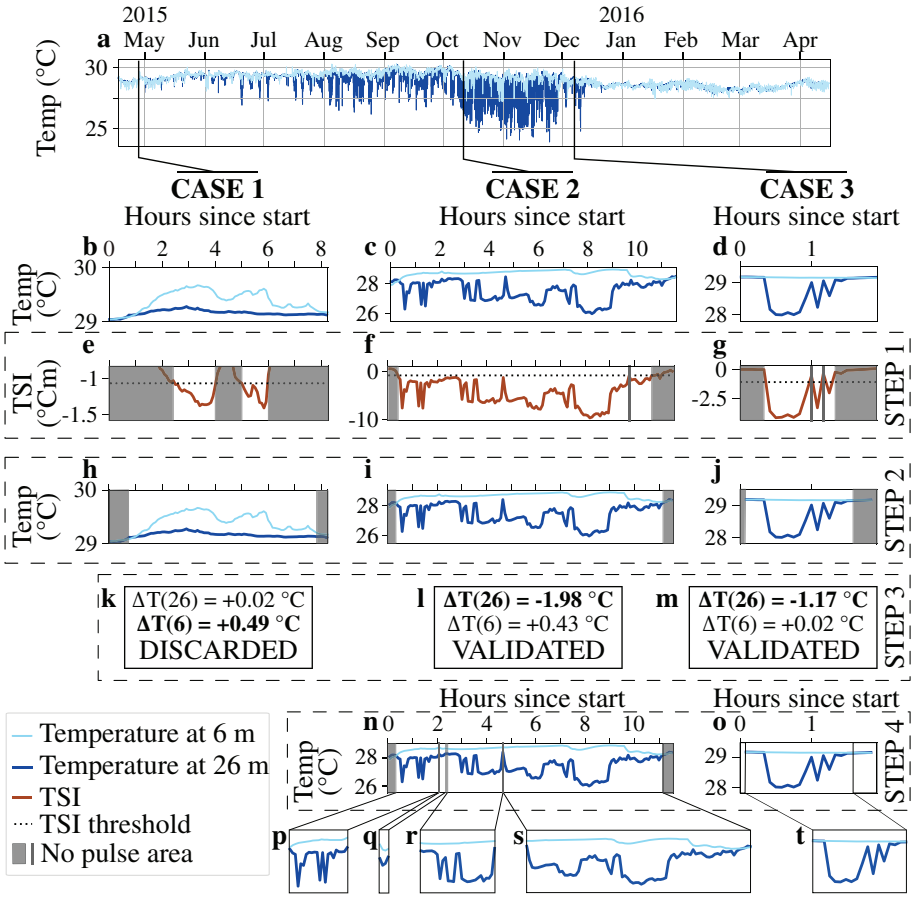

Fig 4. Our automated detection of upwelling-induced cold pulses within subsurface temperature time-series data in shallow tropical environments using a TSI. The figure shows the step-by-step algorithm in three cases. Case 1 (**b**, **e**, **h**, **k**) displays a potential pulse detected linked to heating in the surface layer and discarded by the algorithm. Case 2 (**c**, **f**, **i**, **l**, **n**, **p**–**s**) displays a potential pulse detected containing a series of four successive cold pulses. Case 3 (**d**, **g**, **j**, **m**, **o**, **t**) displays a potential pulse detected containing only one cold pulse. (**a**–**d**) Input temperature data from the northern reef slope at Palmyra Atoll at 6-m (light blue) and 26-m depth (dark blue). (**e**–**g**) Step 1: The TSI (thick solid red line) is computed from the input temperature data and potential pulses are defined as continuous periods of TSI lower than the location-specific threshold (thick dotted line). Hashed areas show where no potential pulse has been detected. (**h**–**j**) Step 2: Boundaries of potential pulses detected are expanded to capture the full extent of the pulses. The figure shows the temperature data of the full potential pulses detected between the hashed areas. (**k**–**m**) Step 3: Potential pulse linked to heating of the surface layer are discarded by the heating filter. The filter computes ΔT for each depth, defined as the difference between the prepulse temperature and the temperature of the minimum TSI. A pulse is discarded if ΔT at the deepest logger is positive (the bottom layer is warming) or if ΔT at the deepest logger does not have the biggest magnitude (shallower layer experienced more temperature changes during the potential pulse). Computed ΔT for 6- and 26-m depth are displayed. The ΔT with the biggest magnitudes are in bold. Potential pulse in Case 1 is discarded, while potential pulses in Case 2 and Case 3 are validated. (**n**–**o**) Step 4: When potential pulses detected and validated by the heating filter contain several successive pulses, they are broken down into individual pulses. (**p**–**t**) Individual cold-pulse events detected by the algorithm.

boundaries in time for each potential pulse. For the new pulse start time, it first computes the last time step before the start of the potential pulse meeting one of three criteria (the TSI is increasing, the TSI is positive, or the deepest logger temperature is not the minimum temperature in the water column). The new start is then defined as the time step right after the one previously computed. Similarly, for the new end time step, it computes the first time step after the end of the potential pulse meeting one of two other criteria (the TSI is positive or the deepest temperature logger is the maximum temperature in the water column). The new end is then defined as the time step before the one previously computed. If potential pulses overlap, they are merged into a single potential cold pulse.

Step 3: Filtering out potential cold pulses linked to surface heating

Because the TSI is based on temperature differences between temperature loggers in a vertical depth array, a potential cold pulse may be recorded due to the water column surface heating instead of the bottom of the water column cooling. Our routine therefore applies a heating filter to all potential pulses to remove those that are not linked to cooling at the deepest logger. This is done for each potential pulse by

computing the temperature difference between the start of the pulse and the time with the minimum TSI (i.e., the maximum TSI magnitude) for each depth. A pulse is authenticated under two conditions. First, the bottom temperature needs to be decreasing between the start of the potential pulse and the time of the minimum TSI. Second, the magnitude of the temperature difference needs to be greater for the bottom logger than for all the other loggers. If one of these conditions is not met, the potential pulse is discarded.

Step 4: Separating successive cold pulses

After the heating filter is applied, a detected pulse might in some cases be a series of successive individual cold pulses in close succession. To identify and separate these, our algorithm applies the following recursive routine, which we call the S-routine.

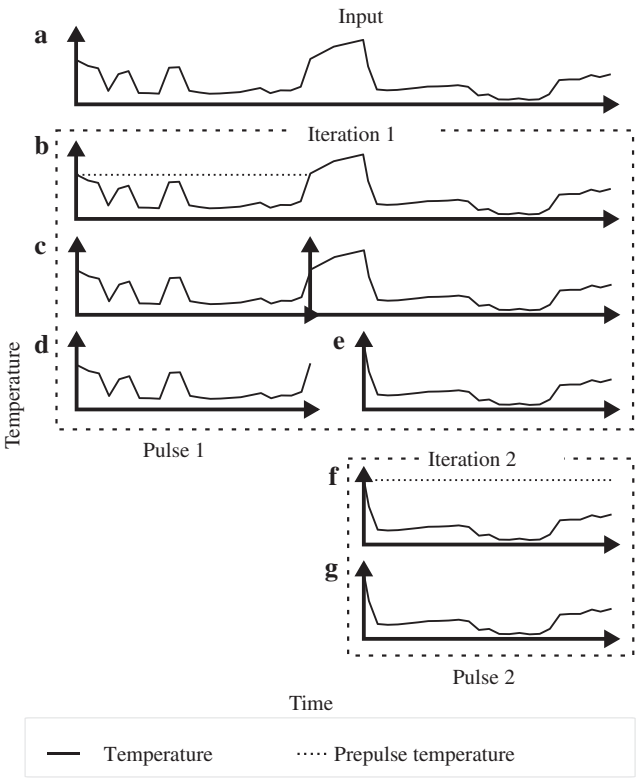

Fig 5. Detailed schematic of our S-routine applied to a hypothetical series of cold pulses. Solid lines represent temperature data over time. Horizontal dotted lines are the prepulse temperature for each step of the routine. (**b**-**e**) The S-routine is applied to the original time series: the end of the first pulse is detected (**b**), the time series is split in two parts (**c**) and the beginning of the following pulse is detected, giving two individual cold pulse times series (**d**-**e**). (**f**-**g**) The S-routine is applied to the new time series (**e**), where no pulse end is detected (**f**) and the time series is validated as an individual cold pulse (**g**). The first real pulse is detected. (**c**) The time series is split into two individual time series. (**d**-**e**) the two extracted time series.

Initialization: The prepulse temperature is defined as the temperature at the first time step of the detected potential pulse (Figs. 5a and 4f).

IF the temperature of the potential pulse remains below the prepulse temperature for the whole duration of the event (Fig. 5f)

- We categorize the potential pulse as an individual event (Fig. 5g) and the S-routine ends.

ELSE (Fig. 4b)

- The potential pulse is split in two parts (Fig. 5c).
- The routine identifies the start of the pulse to when the temperature goes back to the prepulse temperature as an individual cold-pulse event (Fig. 5d).
- The routine then defines the start a new potential pulse within the residual time series. The new potential pulse starts when the bottom logger temperature decreases (Fig. 5e).

IF no such time is found

- The potential pulse is discounted and the S-routine ends.

ELSE

- The S-routine is applied to the new potential pulse (Fig. 5f).

Assessment

To assess the performance of our TSI against the previous CGT methods (Sevadjian et al. 2012; Gove et al. 2015), we built two test datasets by manually identifying cold pulses occurring at 26-m depth in our Palmyra and Wake time-series data. We then analyzed the original unprocessed time-series-data using both the TSI and CGT methods and compared the results to the test data. We defined a true positive (TP) as a time step corresponding to the presence of a pulse that was correctly identified by the TSI and CGT methods. Similarly, we defined a true negative as a time step corresponding to the absence of a pulse that were correctly identified. In contrast, a false positive (FP) was defined as a time step incorrectly identified as a pulse, and a false negative (FN) as a time step where the presence of a pulse failed to be detected. From there, we defined the precision, recall and F_1 score of each method, with the latter classically used for the assessment of anomaly detection algorithms (Anneken et al. 2015; Ji et al. 2019; Li et al. 2020), as in Eqs. 5–7.

$$\text{Recall} = \frac{\text{TP}}{\text{TP} + \text{FN}} \tag{5}$$

$$\text{Precision} = \frac{\text{TP}}{\text{TP} + \text{FP}} \tag{6}$$

$$F_1\text{score} = 2\frac{\text{Precision} \times \text{Recall}}{\text{Precision} + \text{Recall}} \tag{7}$$

Higher recall equates to a higher number of TPs, while higher precision equates to fewer FPs. The F_1 score is affected by both FNs (as in recall) and FPs (as in precision). We consider both errors to matter equally in the process of detecting cold pulses; therefore, we used the F_1 score as a proxy to rank the various detection methods against each other.

Our TSI method requires at least two temperature loggers to be used in an upslope configuration in order to compute the stratification in temperature across the loggers. To quantify upwelling at a certain depth, the TSI computed as in Eq. 3 may be affected by the number of loggers used and their spatial configuration. To test for an effect of the number of loggers and their depth spacing on the TSI values, we assessed the performance of our method in three different ways: first using all three loggers at 6-, 14-, and 26-m depth (called TSI (3) for TSI with three levels), then using the 6- and 26-m loggers (called TSI(2,20) for TSI with two levels, 20 m apart), and finally using the 14- and 26-m loggers (called TSI(2,10) for TSI with two levels, 10 m apart). At Palmyra Atoll, the TSI method achieved an average 92.6% precision, 71.6% recall, and a F_1 score of 80.6% (Table 1). Precision was consistent across the TSI methods and varied from 91.5% to 93.1%. Recall varied more, ranging from 65.7% to 75.7%. The best F_1 score across our three spatial configurations was the TSI(2, 20) (82.9%) and was closely followed by the TSI(3) (82.1%) (Fig. 6a; Table 1). At Wake Atoll, the TSI reached an average precision of 70.4%, recall of 66.3%, and a F_1 score of 68.3%. The best F_1 score across our three spatial configurations was the TSI(3) (70.3%) and was closely followed by the TSI(2,10) (70.2%) (Table 2).

The CGT methods detect cold pulses based on the temporal temperature gradient: if the gradient exceeds a defined threshold (G, in °C min^{-1}), a potential pulse is recorded. If this potential pulse induces a temperature drop greater than a given minimum temperature drop (D, in °C), the potential pulse is considered to be a true cold pulse. The pulse event is considered over when the temperature has recovered to a defined fraction (F, no unit) of the induced temperature drop. If the pulse is longer than a given maximum duration (d, in hours), it is discarded. A given CGT method is thus defined by four parameters and will be referred as CGT (G, D, F, and d). We first assessed the performance of the CGT methods used in Sevadjian et al. (2012) and Gove et al. (2015) corresponding to CGT (G: 0.06, D: 0.3, F: 0.5, d: $+\infty$) and CGT (G: 0.00125, D: 0.3, F: 0.5, d: 13), respectively. To compute the range in precision, recall, and F_1 scores and thus the performance extent of the CGT methods, we varied all four parameters across reasonable ranges. G logarithmically varied from 0.0008°C min^{-1} (minimum detectable gradient using our loggers and sampling frequency) to 0.8°C min^{-1} (near the maximum gradient found in the Palmyra time series: 0.89°C min^{-1}) among 13 values, D varied from 0°C to 1.5°C every 0.1°C, F varied from 0 to 0.9 every 0.1, and d varied across three typical values (13, 24, and 48 h).

At Palmyra, the CGT methods examined showed a wide range in precision (0–100%) and recall (0–97.2%) (Fig. 6a). The highest F_1 score of all CGT methods tested was 72.9%, obtained by the CGT (G: 0.0008, D: 0.1, F: 0.9, d: 24), corresponding to the lowest G, highest F, and filtering pulses below 0.1°C (Table 1). The highest F_1 score of our TSI method applied to the test data was 82.9% and varied between 4.1% and 10.0% higher than the best F_1 scores achieved by the previously published CGT methods, regardless of the CGT method parameter settings (Fig. 6a). Similarly at Wake, the CGT methods spanned a wide range of precision (0–82.1%),

Table 1. Precision, recall, and F_1 scores of our TSI method and previously published CGT method tested on in situ temperature time-series data from Palmyra Atoll, central Pacific. Values in bold represent the best scores reached by either the TSI or CGT method within each method iteration tested.

Method	Precision (%)	Recall (%)	F_1 score (%)
TSI(3)	**93.1**	73.4	82.1
TSI(2,20)	91.5	**75.7**	**82.9**
TSI(2,10)	**93.1**	65.7	77.0
Mean TSI	92.6	71.6	80.6
Best CGT for precision: CGT (G: 0.025, D: 0.9, F: 0.3, d: 24)	**100**	20.1	33.5
Best CGT for recall: CGT (G: 0.0008, D: 0, F: 0, d: 48)	42.0	**97.2**	58.6
Best CGT for F_1 score: CGT (G: 0.0008, D: 0.1, F: 0.9, d: 24)	73.8	72.1	**72.9**
Sevadjian et al. (2012): CGT (G: 0.06, D: 0.3, F: 0.5, d(+inf))	99.5	18.1	30.6
Gove et al. (2015): CGT (G: 0.00125, D: 0.3, F: 0.5, d: 13)	88.9	52.2	65.8

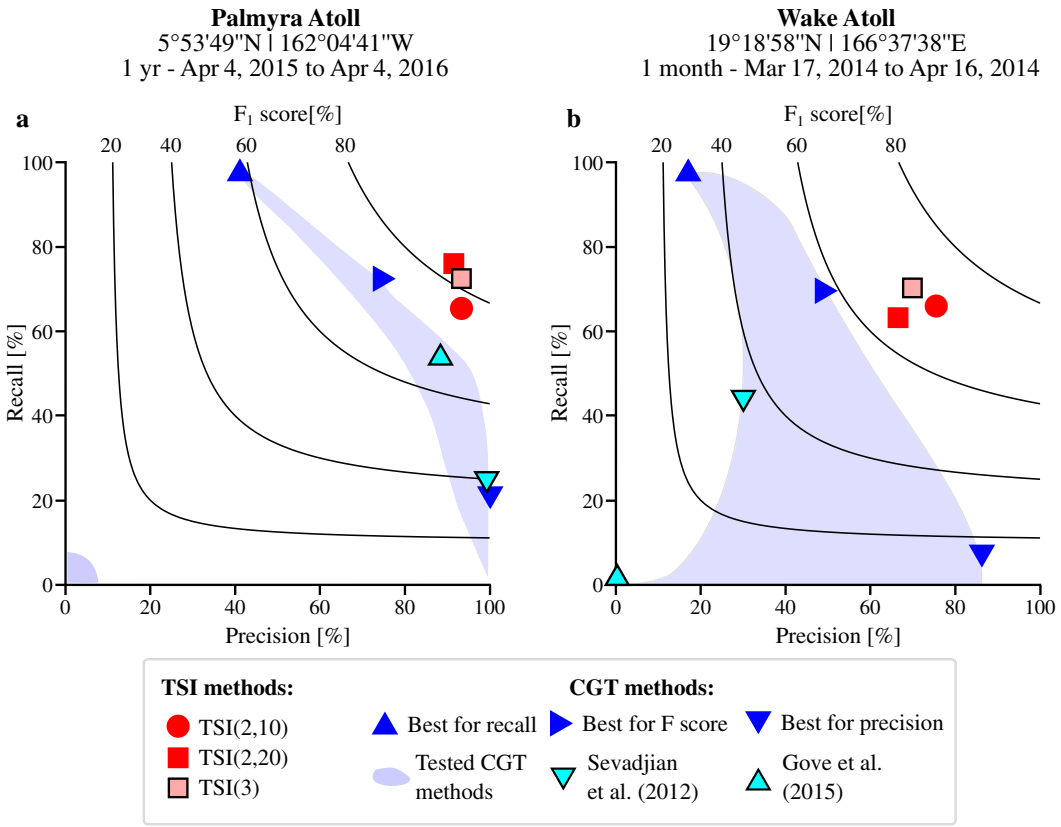

Fig 6. TSI and CGT methods plotted on a precision-recall plane for our study site at Palmyra Atoll (**a**) and Wake Atoll (**b**). Curved lines represent the F_1 score values, increasing from the bottom left corner to the top right corner. All CGT methods are represented by the filled light blue areas and represent a mix of two previously published methods (Sevadjian et al. 2012; Gove et al. 2015) and variations on these that we computed by varying their four user-defined parameters across a reasonable range (see the Assessment section for details).

Table 2. Precision, recall, and F_1 scores of our TSI method and previously published CGT methods tested on in situ temperature time-series data from Wake Atoll, northwestern Pacific. Values in bold represent the best scores reached by either the TSI or CGT method within each method iteration tested. Note the Gove et al. (2015) CGT method did not detect any pulse, hence the recall and precision both equaling zero.

Method	Precision (%)	Recall (%)	F_1 score (%)
TSI(3)	70.6	**70.0**	**70.3**
TSI(2,20)	65.0	63.5	64.2
TSI(2,10)	**75.7**	65.5	70.2
Mean TSI	70.4	66.3	68.3
Best CGT for precision: CGT (*G*: 0.025, *D*: 0.0, *F*: 0.9, *d*: 13)	**82.1**	9.3	16.7
Best CGT for recall: CGT (*G*: 0.0008, *D*: 0, *F*: 0.5, *d*: 48)	17.2	**96.6**	29.3
Best CGT for F_1 score: CGT (*G*: 0.0025, *D*: 0.1, *F*: 0.6, *d*: 13)	46.4	70.7	**56.0**
Sevadjian et al. (2012): CGT (*G*: 0.06, *D*: 0.3, *F*: 0.5, *d*(+inf))	41.8	36.1	38.8
Gove et al. (2015): CGT (*G*: 0.00125, *D*: 0.3, *F*: 0.5, *d*: 13)	0.0	0.0	Not definable

recall (0–96.6%), and F_1 score (0–56.0%). The Sevadjian et al. (2012) method reached an F_1 score of 38.8% while the Gove et al. (2015) method did not detect any pulses in the time series. The best F_1 score was obtained by the CGT (G: 0.0025, D: 0.1, F: 0.6, d: 13) (Table 2). As with the Palmyra test data, the TSI performed better than the best CGT method for all three TSI setups with F_1 scores 12.3–14.3% higher than the best CGT.

Discussion

Gradients in upwelling can have profound effects on the biology and ecology of shallow-water tropical marine communities (Leichter and Genovese 2006; Williams et al. 2018; Aston et al. 2019; Radice et al. 2019; Randall et al. 2020), yet we lack a locally parameterized automated method to quantify the dynamics of such events from in situ temperature time-series data. Here, we developed a novel method, the TSI, that is parameterized based on the local temperature stratification of the water column to quantify subsurface cooling events in stratified waters like those found around tropical coral reef islands. Based on in situ temperature time-series data collected from bed-mounted loggers in an upslope configuration, our method improves on previously published methods by: (1) detecting individual cold-pulse events to allow the computation of summary metrics, (2) removing the need for user-defined input parameters, (3) automatically determining the directional origin of the cold-water mass to isolate cooling as a result of upwelling, and (4) increasing the detection accuracy (F_1 score) by up to 10–14% over previously published methods.

Previously published methods quantify integrated cooling across in situ temperature time-series data (Leichter and Genovese 2006; Wall et al. 2012; Wyatt et al. 2020), but do not identify individual cooling events, preventing the calculation of summary metrics of cold-pulse temporal dynamics. In contrast and like previously published CGT methods (Sevadjian et al. 2012; Gove et al. 2015), our TSI method detects individual cold-pulse events, allowing metrics such as mean pulse duration, mean maximum temperature drop, and mean pulse frequency to be calculated over different temporal windows. Depending on the question at hand, these metrics could be critical. For example, around both continental and oceanic shallow-water tropical coral reefs, cold pulses as a result of deep-water upwelling are associated with increased nutrient supply to the shallows (Leichter et al. 2003; Aston et al. 2019). Cold pulses with a mean short duration could favor macroalgae that are able to capitalize on increased nutrient concentrations in the surrounding waters more rapidly than reef-building corals (Fujita 1985; Raven and Taylor 2003; Ladah et al. 2012; den Haan et al. 2016). In contrast, reef-building corals may benefit where cold pulses occur more frequently or have a longer mean duration. In the central Pacific, the percentage cover of reef-building corals around Jarvis Island peaked where more frequent deep-water cold pulses occurred (Aston et al. 2019), and mean duration of cold pulses associated with night time lagoonal flushing correlated more strongly with coral trophic responses than the total cooling time of these events around Palmyra Atoll (Williams et al. 2018). These ecological responses to specific cold-pulse dynamics would be missed by purely quantifying the summed total amount of cooling over time.

A cold-pulse identification method that requires a priori defined input parameters runs the risk of the user making arbitrary choices or them taking parameter values from previous studies conducted under different environmental contexts. The CGT method used by Sevadjian et al. (2012) and Gove et al. (2015) requires four input parameters to be defined by the user, but our TSI method does not require any predefined input parameters to identify individual cooling events within a temperature time series. Our method defines a "cold pulse" in a geographically context-specific manner based on an already existing dataset (in this case GODAS), which means the operator is not required to have extensive knowledge of the hydrographic properties of the study site. We define a cold pulse as a continuous period of abnormally low TSI, with this criterion based on a climatological threshold of the temperature profile at the study site calculated from the NCEP-GODAS reanalysis product (Behringer and Xue 2004). The TSI cold-pulse detection threshold is therefore automatically tuned for the study site in question, removing biases associated with user-defined input parameter choices. We used the GODAS product because of its continuous 40-yr record and global extent, but other similar gridded products could be used to obtain the long-term climatology. We advise against the use of in situ local temperature records, however, as this would incorporate any effect of seasonal or regular upwelling into the climatology, meaning only the most extreme cold pulses would then be detected by our routine.

In tropical shallow waters, cold pulses can occur in temperature time-series data as a result of surface downwelling in addition to deep-water upwelling (Williams et al. 2018). Despite both mechanisms creating short-term drops in subsurface temperature, the cold-water masses driving the cooling response have fundamentally different origins and may therefore have different effects on shallow-water tropical organisms. Previously, the only way to separate cooling as a result of these different physical mechanisms was the labor-intensive process of manually inspecting each cold pulse identified by the CGT algorithm (Gove et al. 2015; Williams et al. 2018). The TSI method improves on this by automatically separating upwelling from downwelling-induced cooling events by investigating the sign of the temperature gradient along the reef slope. Upwelling-induced cold pulses result in a negative TSI, whereas cold pulses as a result of downwelling result in a positive TSI and are automatically discarded.

As well as solving the core limitations of previously published methods that quantify upwelling-induced cold pulses,

our TSI method shows a substantially increased detection accuracy. Around the shallow tropical waters of Palmyra and Wake Atolls, our TSI method (and its variations tested in terms of number and depth spacing of loggers) achieved an F_1 score 4.1–14.2% better than the best CGT methods, even with the CGT parameters optimized for the test datasets (Tables 1, 2; Fig. 6). There does not seem to be a significant difference in performance between the various TSI setups tested. However, the TSI(2) can be assumed to be better than the TSI(3) as it shows similar results with fewer loggers and therefore reduces equipment cost and labor of logger installation and retrieval.

If two loggers are available, we would advise users to choose the TSI method over any CGT method. Of course, the loggers are required to be of sufficient quality for either method. We advise users to utilize loggers with a high accuracy and a response time to changes in temperature that is far shorter than the duration of the pulses the operator wishes to detect. The depth and relative distance of loggers should also be chosen with care when using our TSI method as results could be affected by the local stratification. For example, if two loggers are too far apart or one is too deep, only one logger might reside in the upper mixed layer. In this case, the background stratification will be high and only the strongest upwelling-induced cold-pulse events may be detected. Similar underestimates are likely to be obtained in a region subject to constant intense upwelling, for example, on the west coast of Jarvis Island that experiences high upwelling intensity and frequency induced by the equatorial undercurrent (Gove et al. 2006; Aston et al. 2019). The use of GODAS data in this case, however, should limit the effects of localized intense upwelling in computing the background temperature stratification.

Users should also consider the risk of placing the loggers too shallow or too close together on the reef slope. In shallow waters, the daily temperature cycle in the atmosphere could bias the results, as pulses producing a smaller temperature difference than the one induced by the warm surface temperature are likely to be discarded during our heating filter processing step. If the two loggers are too close to each other, the temperature drop caused by a cold pulse might occur at both loggers simultaneously, suppressing the temperature gradient required for a pulse to be detected. The absolute distance between the loggers should be at least of the order of magnitude of the cold-pulse propagation celerity multiplied by the sampling frequency. For example, the order of magnitude of the celerity of shoaling internal bores (inducing upwelled cold pulses) is about 10 cm s^{-1} (McSweeney et al. 2020). At a sampling frequency of 300 s (5 min), loggers should be at least 30 m apart to be sure to detect the propagation of such internal bores. As it is likely that most pulses do not travel the shortest path between two loggers, a slightly lower value would be acceptable. In our case, the shallow loggers (15 and 5 m deep) were 24 and 76 m away, respectively, from the deep logger (25 m deep) at Palmyra Atoll and 22 and 66 m away, respectively, from the deep logger at Wake Atoll. With all this in mind, we would advise future users who want to detect cold pulses at a depth d to follow these summary recommendations (note that the depth of detection d corresponds to the depth of the deepest logger): (1) a shallower logger should be used along with the logger at depth d, both mounted to the substrate, (2) both loggers should sit in the upper mixed layer and thus above the thermocline for the duration of the study, (3) the shallow logger should not be too close to the surface to limit the effects of air temperature on the underlying water mass, and (4) the shallow logger should be at a distance in meters of about a 10^{th} of the sampling rate in seconds to create a sufficiently large space to detect cold-pulse propagation. The current work tested these methods using temperature data only. However, in locations where water density is mainly driven by salinity changes, like in the Red Sea, the same methods outlined here could be applied to changes in density stratification (as in Eq. 1) if both salinity and temperature data were available.

In summary, upwelling has several effects on shallow-water tropical communities, but our ability to study these patterns and processes is dependent on our ability to quantify upwelling dynamics in a repeatable and rigorous manner. Importantly, our novel TSI method presented here improves on previously published methods by automatically identifying individual cooling events within a temperature time series without the need for user-defined input parameters. This means our method is easily applied to novel situations to quantify the dynamics of upwelling-induced cooling where previous hydrographic knowledge of the study site is lacking.

References

Alford, M. H., and others. 2015. The formation and fate of internal waves in the South China Sea. Nature **521**: 65–69. doi:10.1038/nature14399

Anneken, M., Y. Fischer & J. Beyerer 2015. Evaluation and comparison of anomaly detection algorithms in annotated datasets from the maritime domain. IntelliSys 2015 - Proceedings of 2015 SAI Intelligent Systems Conference. Institute of Electrical and Electronics Engineers Inc. 169–178. doi:10.1109/IntelliSys.2015.7361141

Aston, E. A., and others. 2019. Scale-dependent spatial patterns in benthic communities around a tropical island seascape. Ecography **42**: 578–590. doi:10.1111/ecog.04097

Behringer, D. and Y. Xue 2004. Evaluation of the global ocean data assimilation system at NCEP: The Pacific Ocean. Proceedings of the Eighth International Symposium on Integrated Observing and Assimilation Systems for Atmosphere, Oceans, and Land Surface. 11–15.

Comfort, C. M., G. O. Walker, M. A. McManus, A. G. Fujimura, C. E. Ostrander, and T. J. Donaldson. 2019. Physical dynamics of the reef flat, channel, and fore reef areas of

a fringing reef embayment: An oceanographic study of Pago Bay, Guam. Reg. Stud. Mar. Sci. **31**: 100740. doi:10.1016/j.rsma.2019.100740

Fujita, R. M. 1985. The role of nitrogen status in regulating transient ammonium uptake and nitrogen storage by macroalgae. J. Exp. Mar. Biol. Ecol. **92**: 283–301. doi:10.1016/0022-0981(85)90100-5

Gove, J. M., M. A. Merrifield, and R. E. Brainard. 2006. Temporal variability of current-driven upwelling at Jarvis Island. J. Geophys. Res. Oceans **111**: C12011. doi:10.1029/2005JC003161

Gove, J. M., G. J. Williams, M. A. Mcmanus, S. J. Clark, J. S. Ehses, and L. M. Wedding. 2015. Coral reef benthic regimes exhibit non-linear threshold responses to natural physical drivers. Mar. Ecol. Prog. Ser. **522**: 33–48. doi:10.2307/24895091

den Haan, J., Huisman, J., Brocke, H., et al. 2016. Nitrogen and phosphorus uptake rates of different species from a coral reef community after a nutrient pulse. Sci. Rep. **6**: 28821. doi:10.1038/srep28821

Ji, C., X. Zou, S. Liu, and L. Pan. 2019. ADARC: An anomaly detection algorithm based on relative outlier distance and biseries correlation. Software Pract. Exper. **50**: 2065–2081. doi:10.1002/spe.2756

Ladah, L. B., A. Filonov, M. F. Lavín, J. J. Leichter, J. A. Zertuche-González, and D. M. Pérez-Mayorga. 2012. Cross-shelf transport of sub-thermocline nitrate by the internal tide and rapid (3-6h) incorporation by an inshore macroalga. Cont. Shelf Res. **42**: 10–19. doi:10.1016/j.csr.2012.03.010

Leichter, J. J., and S. J. Genovese. 2006. Intermittent upwelling and subsidized growth of the scleractinian coral *Madracis mirabilis* on the deep fore-reef slope of Discovery Bay, Jamaica. Mar. Ecol. Prog. Ser. **316**: 95–103. doi:10.3354/meps316095

Leichter, J. J., and others. 2003. Episodic nutrient transport to Florida coral reefs. Limnol. Oceanogr. **48**: 1394–1407. doi:10.4319/lo.2003.48.4.1394

Leichter, J. J., S. R. Wing, S. L. Miller, and M. W. Denny. 1996. Episodic nutrient transport to Florida coral reefs for logistic support. Limnol. Oceanogr. **41**: 1490–1501. doi:10.4319/lo.2003.48.4.1394

Li, Y., X. Zhong, Z. Ma, and H. Liu. 2020. The outlier and integrity detection of rail profile based on profile registration. IEEE Trans. Intell. Transp. Syst. **21**: 1074–1085. doi:10.1109/TITS.2019.2901633

McSweeney, J. M., and others. 2020. Observations of shoaling nonlinear internal bores across the central California inner shelf. J. Phys. Oceanogr. **50**: 111–132. doi:10.1175/JPO-D-19-0125.1

McPhaden, M. J., S. E. Zebiak, and M. H. Glantz. 2006. ENSO as an integrating concept in earth science. Science (80-) **314**: 1740–1745. doi:10.1126/science.1132588

Monismith, S. G., A. Genin, M. A. Reidenbach, G. Yahel, and J. R. Koseff. 2006. Thermally driven exchanges between a coral reef and the adjoining ocean. J. Phys. Oceanogr. **36**: 1332–1347. doi:10.1175/JPO2916.1

Pacherres, C. O., G. M. Schmidt, and C. Richter. 2013. Autotrophic and heterotrophic responses of the coral *Porites lutea* to large amplitude internal waves. J. Exp. Biol. **216**: 4365–4374. doi:10.1242/jeb.085548

Pineda, J. 1991. Predictable upwelling and the shoreward transport of planktonic larvae by internal tidal bores. Science **253**: 548–549. doi:10.1126/science.253.5019.548

Radice, V. Z., O. Hoegh-Guldberg, B. Fry, M. D. Fox, and S. G. Dove. 2019. Upwelling as the major source of nitrogen for shallow and deep reef-building corals across an oceanic atoll system. Funct. Ecol. **33**: 1120–1134. doi:10.1111/1365-2435.13314

Randall, C. J., Toth, L. T., Leichter, J. J., Maté, J. L., and Aronson, R. B. 2020. Upwelling buffers climate change impacts on coral reefs of the eastern tropical Pacific. Ecology **101**(2): e02918. doi:10.1126/science.253.5019.548

Rao, R. R., and R. Sivakumar. 2000. Seasonal variability of near-surface thermal structure and heat budget of the mixed layer of the tropical Indian Ocean from a new global ocean temperature climatology. J. Geophys. Res. Oceans **105**: 995–1015. doi:10.1029/1999jc900220

Raven, J. A., and R. Taylor. 2003. Macroalgal growth in nutrient-enriched estuaries: A biogeochemical and evolutionary perspective. Water Air Soil Pollut. Focus **3**: 7–26. doi:10.1023/A:1022167722654

Reid, E. C., T. M. DeCarlo, A. L. Cohen, G. T. F. Wong, S. J. Lentz, A. Safaie, A. Hall, and K. A. Davis. 2019. Internal waves influence the thermal and nutrient environment on a shallow coral reef. Limnol. Oceanogr. **64**: 1949–1965. doi:10.1002/lno.11162

Roder, C., L. Fillinger, C. Jantzen, G. M. Schmidt, S. Khokiattiwong, and C. Richter. 2010. Trophic response of corals to large amplitude internal waves. Mar. Ecol. Prog. Ser. **412**: 113–128. doi:10.3354/meps08707

Safaie, A., and others. 2018. High frequency temperature variability reduces the risk of coral bleaching. Nat. Commun. **9**: 1671. doi:10.1038/s41467-018-04074-2

Schmidt, G. M., M. Wall, M. Taylor, C. Jantzen, and C. Richter. 2016. Large-amplitude internal waves sustain coral health during thermal stress. Coral Reefs **35**: 869–881. doi:10.1007/s00338-016-1450-z

Sevadjian, J. C., M. A. McManus, K. J. Benoit-Bird, and K. E. Selph. 2012. Shoreward advection of phytoplankton and vertical re-distribution of zooplankton by episodic near-bottom water pulses on an insular shelf: Oahu, Hawaii. Cont. Shelf Res. **50–51**: 1–15. doi:10.1016/j.csr.2012.09.006

Simpson, J. H., and R. D. Pingree. 1978. Shallow sea fronts produced by tidal stirring, p. 29–42. *In* Oceanic fronts in coastal processes, Springer.

Wall, M., G. M. Schmidt, P. Janjang, S. Khokiattiwong, and C. Richter. 2012. Differential impact of monsoon and large

amplitude internal waves on coral reef development in the Andaman Sea. PLoS One **7**: e50207. doi:10.1371/journal.pone.0050207

Walter, R. K., C. B. Woodson, P. R. Leary, and S. G. Monismith. 2014. Connecting wind-driven upwelling and offshore stratification to nearshore internal bores and oxygen variability. J. Geophys. Res. Oceans **119**: 3517–3534. doi:10.1002/2014JC009998

Williams, G. J., and others. 2018. Biophysical drivers of coral trophic depth zonation. Mar. Biol. **165**: 60. doi:10.1007/s00227-018-3314-2

Woodson, C. B. 2018. The fate and impact of internal waves in nearshore ecosystems. Ann. Rev. Mar. Sci. **10**: 421–441. doi:10.1146/annurev-marine-121916

Wyatt, A. S. J., J. J. Leichter, L. T. Toth, T. Miyajima, R. B. Aronson, and T. Nagata. 2020. Heat accumulation on coral reefs mitigated by internal waves. Nat. Geosci. **13**: 28–34. doi:10.1038/s41561-019-0486-4

Acknowledgments

The NCEP-GODAS in-depth temperature data were provided by the NOAA/OAR/ESRL Physical Science Laboratory (Boulder, Colorado, USA), and downloaded from their Website at https://psl.noaa.gov/. Subsurface in situ temperature data used for the assessment and the method development were provided by the NOAA/PIFSC/RAMP, Ecosystem Science Division. A python package including the code of the temperature stratification index method is available online at https://github.com/rguilcas/cold_pulses/blob/master/README.md.

Conflict of Interest

None declared.

Submitted 07 August 2020
Revised 02 March 2021
Accepted 08 July 2021

Associate editor: Craig Lee